https://doi.org/10.1016/j.msea.2017.02.069

This is the Pre-Published Version.

Author’s Accepted Manuscript

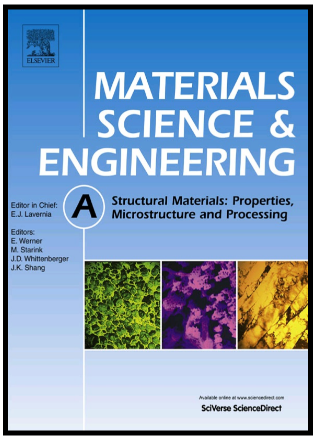

www.elsevier.com/locate/msea

Micromechanics-based Damage Model for Failure Prediction in Cold Forming

X.Z. Lu, L.C. Chan

PII: S0921-5093(17)30228-9
DOI: http://dx.doi.org/10.1016/j.msea.2017.02.069
Reference: MSA34745

To appear in: *Materials Science & Engineering A*

Received date: 8 December 2016
Revised date: 17 February 2017
Accepted date: 18 February 2017

Cite this article as: X.Z. Lu and L.C. Chan, Micromechanics-based Damag Model for Failure Prediction in Cold Forming, *Materials Science & Engineerin A,* http://dx.doi.org/10.1016/j.msea.2017.02.069

This is a PDF file of an unedited manuscript that has been accepted fo publication. As a service to our customers we are providing this early version o the manuscript. The manuscript will undergo copyediting, typesetting, an review of the resulting galley proof before it is published in its final citable forn Please note that during the production process errors may be discovered whic could affect the content, and all legal disclaimers that apply to the journal pertain

© 2017. This manuscript version is made available under the CC-BY-NC-ND 4.0 license http://creativecommons.org/licenses/by-nc-nd/4.0/

ACCEPTED MANUSCRIPT

Micromechanics-based Damage Model for Failure Prediction in Cold Forming

X.Z. Lu, L.C. Chan*

Department of Industrial and Systems Engineering, The Hong Kong Polytechnic University, Hung Hom, Kowloon, Hong Kong S.A.R., China

*Corresponding author

Tel.: +852 2766 6634

Fax: +852 2766 6771

E-mail addresses: lc.chan@polyu.edu.hk

Accepted manuscript

ACCEPTED MANUSCRIPT

Abstract

The purpose of this study was to develop a micromechanics-based damage (micro-damage) model that was concerned with the evolution of micro-voids for failure prediction in cold forming. Typical stainless steel SS316L was selected as the specimen material, and the nonlinear isotropic hardening rule was extended to describe the large deformation of the specimen undergoing cold forming. A micro-focus high-resolution X-ray computed tomography (CT) system was employed to trace and measure the micro-voids inside the specimen directly. Three-dimensional (3D) representative volume element (RVE) models with different sizes and spatial locations were reconstructed from the processed CT images of the specimen, and the average size and volume fraction of micro-voids (VFMV) for the specimen were determined via statistical analysis. Subsequently, the micro-damage model was compiled as a user-defined material subroutine into the finite element (FE) package ABAQUS. The stress-strain responses and damage evolutions of SS316L specimens under tensile and compressive deformations at different strain rates were predicted and further verified experimentally. It was concluded that the proposed micro-damage model is convincing for failure prediction in cold forming of the SS316L material.

Accepted manuscript

Keywords: Micromechanics-based damage model; X-ray computed tomography; Representative volume element; Failure prediction; Large deformation; Cold forming.

ACCEPTED MANUSCRIPT

Nomenclature

$\mathbf{F}$	Deformation gradient tensor
$\mathbf{R}$	Rotation tensor with orthogonality
$\mathbf{h}$	Hencky's logarithmic strain
$\mathbf{h}^{\mathrm{e}}$, $\mathbf{h}^{\mathrm{p}}$	Elastic and plastic strain tensors respectively
$\mathbf{D}$	Stretching tensor
$\mathbf{D}^{\mathrm{e}}$, $\mathbf{D}^{\mathrm{p}}$	Elastic and plastic stretching tensors respectively
E	Elastic modulus
ν	Poisson's ratio
$\boldsymbol{\tau}$	Kirchhoff stress tensor
$\mathbf{D}^{\mathrm{p}\prime}$	Deviatoric stress tensor
$\mathbf{D}^{\mathrm{p}(\mathrm{m})}$	Hydrostatic stress tensor
f	Volume fraction of micro-voids (VFMV)
ρ	Specific density of the material
p	Accumulated plastic strain
$\dot{p}$	Accumulated plastic strain rate
n, K	Material viscosity constants
$\langle\ \rangle$	McCauley operator
$\mathbf{N}$	Unit normal vector of the yield surface
F_y	Yield surface
s_i, i=1, 2	Damage parameters
Q	Isotropic hardening deformation resistance
R^{sat}	Saturated stress value
β	Evolution rate of R

Accepted manuscript

ACCEPTED MANUSCRIPT

1. Introduction

The identification of damage initiation and evolution is always a key concern in the metal forming process [1]. Classical damage theory is based on the continuum mechanics-based thermodynamics framework initiated by Kachanov, Lemaitre and Chaboche [2-5], which is known as continuum damage mechanics (CDM). Following on the basic concept of effective stress, researchers have paid much attention to the application of the CDM approach in different material forming or loading conditions. Wang [6] developed a unified nonlinear damage evolution rule for ductile materials. By using two damage state variables, Chaboche et al. [7] proposed a modified CDM model to describe the plastic compressibility in ductile damage. Pires et al. [8] improved the original CDM model by incorporating the micro-crack closure effect to predict the damage growth and fracture initiation in ductile materials. Soyarslan and Tekkaya [9] developed a modified CDM model coupled with multiplicative finite plasticity to study the propagation of inner defects in forward extrusion. However, although this phenomenological CDM model saves computational time, it ignores the physical details, e.g., micro-defects, of the material [10-12].

Thus, another approach, the micromechanics-based damage (micro-damage) model, which considers the effects of void initiation and evolution, was developed and brought to the front as a popular research topic. This approach was originally developed by Gurson [13] and known as the GTN model [13-15]. In the GTN model, ductile fracture occurs through the void nucleation, growth, and coalescence. The void coalescence is the final stage in the fracture of ductile materials. It can be triggered by localized plastic deformation inside the inter-void ligament between neighbouring voids and can be modelled by accelerating void growth at a critical void volume fraction. Needleman and Tvergaard [14] improved the GTN model by taking into

Accepted manuscript

account the void evolution and material strain hardening. In order to describe the ductile materials with irregular-shaped voids, Gologanu and Leblond [16] extended the GTN model based on an “expansion” velocity field condition. By considering the void shape, void location, strain hardening and stress triaxiality, Pardoen and Hutchinson [17] enhanced the GTN model to establish the criterion of void coalescence.

In the application of the micro-damage model for damage prediction [11, 18], the identification of micro-void initiation and growth is of great importance. For micro-voids detection, destructive methods are used commonly to measure its interior distribution. In addition, the VFMV is always evaluated by quantitative metallographic analysis or microscopic examinations [18-21]. However, such testing procedures are destructive, and it is unimaginably difficult to locate the cross-sections and obtain other useful information from numerous micro-voids accurately. In view of this, X-ray CT is an ideal alternative technique that avoids material destruction and allows for superior image quality of the inner microstructure [22]. It is not only for image capturing and generating external 3D profiles, but also for visualizing internal features of solid objects. Digital volumetric data of the tested specimens can be obtained simultaneously by the high-end data-analysis and visualization software, so as to obtain more reliable information, such as the spatial location, size, compactness, and sphericity, etc., of micro-voids. This enables more accurate calculation of the void volume fraction [23, 24]. It is a very powerful tool to realize and support the material microstructure characterization as well as high-resolution micro-interior reverse engineering for various applications such as high-precision engineering, defect detection, composite material science, dimensional metrology and other potential applications [25].

Accepted manuscript

ACCEPTED MANUSCRIPT

The above phenomenological CDM or micro-damage models are always implemented in finite element (FE) packages for damage prediction of metallic materials. However, the application of the X-ray CT technique for damage parameter identification in the micro-damage model has rarely been studied. Also, most of the mentioned constitutive models coupled with damage were formulated within the small deformation framework, which limited their applications in the large deformation processes of metallic materials with good plasticity [26, 27].

Thus, the main objective of this study was to develop a micro-damage model framework for failure prediction in the large deformation of metallic material undergoing cold forming. Typical stainless steel SS316L, which possesses good ductility, high strength and superior corrosion resistance [28], was selected as the specimen material for the X-ray CT scanning and uniaxial tension and compression tests. A micro-focus high-resolution X-ray CT system was employed specially to trace and measure the micro-voids of the specimen directly. In which, the micro-voids inside the material can be modelled precisely and accurately. Furthermore, 3D RVE models with different sizes and spatial locations were reconstructed and the average size and VFMV for the specimen were determined via statistical analysis. Subsequently, the aforesaid micro-damage model was compiled as a user-defined subroutine into ABAQUS. The stress-strain responses and damage evolution in cold forming of SS316L were predicted and further verified experimentally.

Accepted manuscript

2. Micromechanics-based damage model

In this section, a micromechanics-based damage model describing the large deformation behaviour of metallic material was presented. The specific constitutive equations of the micro-damage model based on hypo-elastic relations were derived

ACCEPTED MANUSCRIPT

[17, 29]. In order to describe the elasto-plastic behaviour of metallic materials, the additive decomposition of the Hencky's logarithmic strain **h** is defined as [30]

$$\mathbf{h} = \mathbf{h}^{\mathrm{e}} + \mathbf{h}^{\mathrm{p}}, \tag{1}$$

Where $\mathbf{h}^{\mathrm{e}}$ and $\mathbf{h}^{\mathrm{p}}$ are the elastic and plastic strain tensors respectively.

For large deformation conditions, the logarithmic strain **h** can be replaced by stretching tensor **D** as

$$\mathbf{D} = \mathbf{D}^{\mathrm{e}} + \mathbf{D}^{\mathrm{p}}, \tag{2}$$

where $\mathbf{D}^{\mathrm{e}}$ and $\mathbf{D}^{\mathrm{p}}$ are the elastic and plastic stretching tensors, respectively. Further, the elastic strain tensor $\mathbf{h}^{\mathrm{e}}$ can be assumed as a state variable to formulate the constitutive equations, and it conforms to the following expression

$$\mathbf{D}^{\mathrm{e}} = \overset{\circ}{\mathbf{h}}{}^{\log(\mathrm{e})}. \tag{3}$$

The elastic stretching tensors $\mathbf{D}^{\mathrm{e}}$ can be formulated by the hypo-elastic relationship as [30]

$$\mathbf{D}^{\mathrm{e}} = \frac{1+\nu}{E}\overset{\circ}{\boldsymbol{\tau}}{}^{\log} - \frac{\nu}{E}\operatorname{tr}(\dot{\boldsymbol{\tau}})\mathbf{1}, \tag{4}$$

where ν and E are Poisson's ratio and elastic modulus, respectively, and $\boldsymbol{\tau}$ is the Kirchhoff stress tensor.

The plastic stretching tensors $\mathbf{D}^{\mathrm{p}}$ can be decomposed into two parts, i.e., the deviatoric stress tensor $\mathbf{D}^{\mathrm{p}\prime}$ and the hydrostatic stress tensor $\mathbf{D}^{\mathrm{p(m)}}$,

$$\mathbf{D}^{\mathrm{p}} = \mathbf{D}^{\mathrm{p}\prime} + \mathbf{D}^{\mathrm{p(m)}} = \mathbf{D}^{\mathrm{p}\prime} + \frac{1}{3}\operatorname{tr}\left(\mathbf{D}^{\mathrm{p}}\right)\mathbf{1}. \tag{5}$$

By introducing the concept of volume fraction of micro-voids $f = 1-\rho$ (where ρ is the specific density of a given material), the flow rules $\mathbf{D}^{\mathrm{p}\prime}$ and $\mathbf{D}^{\mathrm{p(m)}}$ can be assumed as [19]

Accepted manuscript

ACCEPTED MANUSCRIPT

$$\mathbf{D}^{\mathrm{p}\prime} = \sqrt{\frac{3}{2}}\dot{p}\mathbf{N} = \sqrt{\frac{3}{2}}\left\langle \frac{F_y}{K} \right\rangle^n \mathbf{N}, \tag{6}$$

$$\mathbf{D}^{\mathrm{p(m)}} = \frac{1}{3} f s_1 \exp\left(\frac{\mathrm{tr}(\boldsymbol{\tau})}{3 s_2 \rho} \right) \dot{p}\mathbf{1}, \tag{7}$$

where $\dot{p}$ is the accumulated plastic strain rate, n and K are the material viscosity constants. s_1 and s_2 are damage parameters, $\langle\ \rangle$ is the McCauley operator; $\mathbf{N} = \frac{\boldsymbol{\tau}'}{\|\boldsymbol{\tau}'\|}$ is the unit normal vector of the yield surface F_y.

The yield surface of F_y can be expressed as [31]

$$F_y = \sqrt{\frac{3}{2}}\|\boldsymbol{\tau}'/\rho\| + f s_1 s_2 \exp\left(\frac{\mathrm{tr}(\boldsymbol{\tau})}{3 s_2 \rho} \right) - Q, \tag{8}$$

where Q is the isotropic hardening deformation resistance with the following specific form

$$Q = Q_0 + R, \tag{9}$$

where Q_0 and R are the initial deformation resistance and the subsequent resistance, respectively.

The evolution law of the resistance R can be formulated as

$$\dot{R} = \beta\left(R^{\mathrm{sat}} - R\right)\dot{p}, \tag{10}$$

where R^{sat} is the saturated value of R, β controls the evolution rate of R.

According to effective stress concept of damage mechanics [2] and mass conservation [19, 20], the damage evolution law of the material can be expressed by the evolution of VFMV f as

$$\dot{f} = \rho\,\mathrm{tr}\left(\mathbf{D}^{\mathrm{p}}\right) = \rho f s_1 \exp\left(\frac{\mathrm{tr}(\boldsymbol{\tau})}{3 s_2 \rho} \right) \dot{p}. \tag{11}$$

The expression of the driving force is

Accepted manuscript

ACCEPTED MANUSCRIPT

$$F_f = \frac{s_2}{\rho_0} \ln\left(\frac{f\left(1-f_0\right)}{f_0\left(1-f\right)} \right). \tag{12}$$

3. Finite element implementations

The proposed micro-damage model was implemented into the ABAQUS using the subroutine UMAT which allows the strain and stress from intrinsic dissipation to be calculated at each integration point. Based on the backward Euler method and radial return [31-34], the implicit stress integration algorithm has been proposed in this study.

3.1. Discretization of constitutive equations

First, an initial state of the moment *t*=0 is considered, i.e.,

$$\boldsymbol{\tau}\big|_{t=0} = \mathbf{0}, \quad \mathbf{F}\big|_{t=0} = \mathbf{R}^{\log}\big|_{t=0} = \mathbf{1} \tag{13}$$

At the time interval from steps n to n+1 with a time increment $\Delta t = t_{n+1} - t_n$, the Kirchhoff stress tensor $\boldsymbol{\tau}_{n+1}$ can be obtained such that

$$\boldsymbol{\tau}_{n+1} = \overset{\circ}{\boldsymbol{\tau}}{}^{\log}_{n+1} \Delta t + \Delta\mathbf{R}_{n+1} \boldsymbol{\tau}_n \Delta\mathbf{R}^{\mathrm{T}}_{n+1}. \tag{14}$$

In addition, the evolution equations of hypo-elastic relation, yield function, viscoplastic flow rule, density and VFMV can be discretized as

$$\overset{\circ}{\boldsymbol{\tau}}{}^{\log}_{n+1} = \rho_{n+1} \mathbb{D} : \mathbf{D}^{\mathrm{e}}_{n+1} \Delta t + \frac{\Delta\rho_{n+1}}{\rho_{n+1}} \boldsymbol{\tau}_{n+1}, \tag{15}$$

Where $\mathbb{D}$ is the fourth-order elastic tensor.

$$F_{y(n+1)} = \sqrt{\frac{3}{2}} \left\| \boldsymbol{\tau}'_{n+1} / \rho_{n+1} \right\| + f_{n+1} s_1 s_2 \exp\left(\frac{\mathrm{tr}\left(\boldsymbol{\tau}_{n+1}\right)}{3 s_2 \rho_{n+1}} \right) - Q_{n+1}. \tag{16}$$

Accepted manuscript

ACCEPTED MANUSCRIPT

$$\left(\mathbf{D}_{n+1}^{\mathrm{p}}\right)' = \frac{\sqrt{\frac{3}{2}}\Delta p_{n+1}\mathbf{N}_{n+1}}{\Delta t}. \tag{17}$$

$$\mathbf{D}_{n+1}^{\mathrm{p(m)}} = \frac{1}{3} f_{n+1} s_1 \exp\left(\frac{\mathrm{tr}\left(\boldsymbol{\tau}_{n+1}\right)}{3 s_2 \rho}\right)\frac{\Delta p_{n+1}}{\Delta t}\mathbf{1}. \tag{18}$$

$$\Delta p_{n+1} = \left\langle \frac{F_{y(n+1)}}{K} \right\rangle^{n} \Delta t. \tag{19}$$

$$\Delta \rho_{n+1} = -\Delta f_{n+1}. \tag{20}$$

$$\Delta f_{n+1} = \rho_{n+1} f_{n+1} s_1 \exp\left(\frac{\mathrm{tr}\left(\boldsymbol{\tau}_{n+1}\right)}{3 s_2 \rho_{n+1}}\right)\Delta p_{n+1}, \tag{21}$$

with

$$\mathbf{N}_{n+1} = \frac{\boldsymbol{\tau}'_{n+1}}{\left\|\boldsymbol{\tau}'_{n+1}\right\|} \qquad \left(\mathbf{N}_{n+1} : \mathbf{N}_{n+1} = 1 \quad \text{when} \quad F_{y(n+1)} = 0\right). \tag{22}$$

$$Q_{n+1} = Q_n + \Delta R_{n+1}, \tag{23}$$

where

$$\Delta R_{n+1} = \beta\left(R_{sat} - R_n\right)\Delta p_{n+1}. \tag{24}$$

3.2. Implicit stress integration algorithm

The implicit stress integration algorithm is illustrated in Fig. 1. For the given values of $\Delta \mathbf{F}_{n+1}$ and Δt_{n+1}, assuming that the variables of $\boldsymbol{\tau}_n$, ρ_n, $\mathbf{F}_n$ and $\mathbf{R}_n^{\log}$ at time t_n have been obtained, variable $\boldsymbol{\tau}_{n+1}$ at time t_{n+1} can be solved by adopting the approach of elastic-prediction and plastic-correction [32, 33].

Assuming that the deformation increment at time t_{n+1} is elastic, the trial variables, i.e., $\boldsymbol{\tau}_{n+1}^{*}$, ρ_{n+1}^{*}, Q_{n+1}^{*}, $(F_y)_{n+1}^{*}$, in the step n+1 can be obtained.

If

Accepted manuscript

ACCEPTED MANUSCRIPT

$$F^{*}_{y(n+1)} \le 0, \tag{25}$$

means the yield is not reached at a given increment step. The trial stress state is the true state. Otherwise, plastic yield occurred and Eq. (14) can be rewritten as

$$\boldsymbol{\tau}_{n+1} = \frac{\rho_{n+1}}{\rho_n}\left(\frac{\rho_{n+1}}{\rho_n}\boldsymbol{\tau}^{*}_{n+1} - \rho_{n+1}\mathbb{D}:\mathbf{D}^{\mathrm{p}}_{n+1}\Delta t - \frac{\Delta\rho_{n+1}}{\rho_n}\Delta\mathbf{R}_{n+1}\boldsymbol{\tau}_n\Delta\mathbf{R}^{\mathrm{T}}_{n+1}\right). \tag{26}$$

The deviation of Eq. (26) is given as

$$\boldsymbol{\tau}'_{n+1} = \frac{\rho^2_{n+1}}{\rho^2_n}\boldsymbol{\tau}'^{*}_{n+1} - 2\mu\frac{\rho_{n+1}}{\rho_n}\mathbf{D}^{\mathrm{p}}_{n+1}\Delta t - \frac{\Delta\rho_{n+1}\rho_{n+1}}{\rho^2_n}\left(\Delta\mathbf{R}_{n+1}\boldsymbol{\tau}_n\Delta\mathbf{R}^{\mathrm{T}}_{n+1}\right)'. \tag{27}$$

Then the yield function is

$$\begin{aligned}\left\|\boldsymbol{\tau}'_{n+1}\right\| = {}& \left\|\frac{\rho^2_{n+1}}{\rho^2_n}\boldsymbol{\tau}'^{*}_{n+1} - \frac{\Delta\rho_{n+1}\rho_{n+1}}{\rho^2_n}\left(\Delta\mathbf{R}_{n+1}\boldsymbol{\tau}_n\Delta\mathbf{R}^{\mathrm{T}}_{n+1}\right)'\right\| - \\ & 2\mu\frac{\rho_{n+1}}{\rho_n}\left(\sqrt{\frac{3}{2}} + \frac{1}{3}f_{n+1}s_1\exp\left(\frac{\mathrm{tr}\left(\boldsymbol{\tau}_{n+1}\right)}{3s_2\rho_{n+1}}\right)\right)\Delta p_{n+1}\end{aligned}. \tag{28}$$

Thus, the following nonlinear scalar equation can be obtained

$$\begin{aligned}&\bar{Y}_{n+1} - \bar{Y}^{*}_{n+1} + 3\mu\frac{\rho_{n+1}}{\rho_n}\left(1 + \sqrt{\frac{1}{6}}f_{n+1}s_1\exp\left(\frac{\mathrm{tr}\left(\boldsymbol{\tau}_{n+1}\right)}{3s_2\rho_{n+1}}\right)\right) \\ &\left\langle\frac{\dfrac{\bar{Y}_{n+1}}{\rho_{n+1}} + f_{n+1}s_1s_2\exp\left(\dfrac{\mathrm{tr}\left(\boldsymbol{\tau}_{n+1}\right)}{3s_2\rho_{n+1}}\right) - Q_{n+1}}{K}\right\rangle^{n}\Delta t = 0,\end{aligned} \tag{29}$$

where $\bar{Y}_{n+1} = \left\|\boldsymbol{\tau}'_{n+1}\right\|$, $\bar{Y}^{*}_{n+1} = \left\|\frac{\rho^2_{n+1}}{\rho^2_n}\boldsymbol{\tau}'^{*}_{n+1} - \frac{\Delta\rho_{n+1}\rho_{n+1}}{\rho^2_n}\left(\Delta\mathbf{R}_{n+1}\boldsymbol{\tau}_n\Delta\mathbf{R}^{\mathrm{T}}_{n+1}\right)'\right\|$.

Accepted manuscript

ACCEPTED MANUSCRIPT

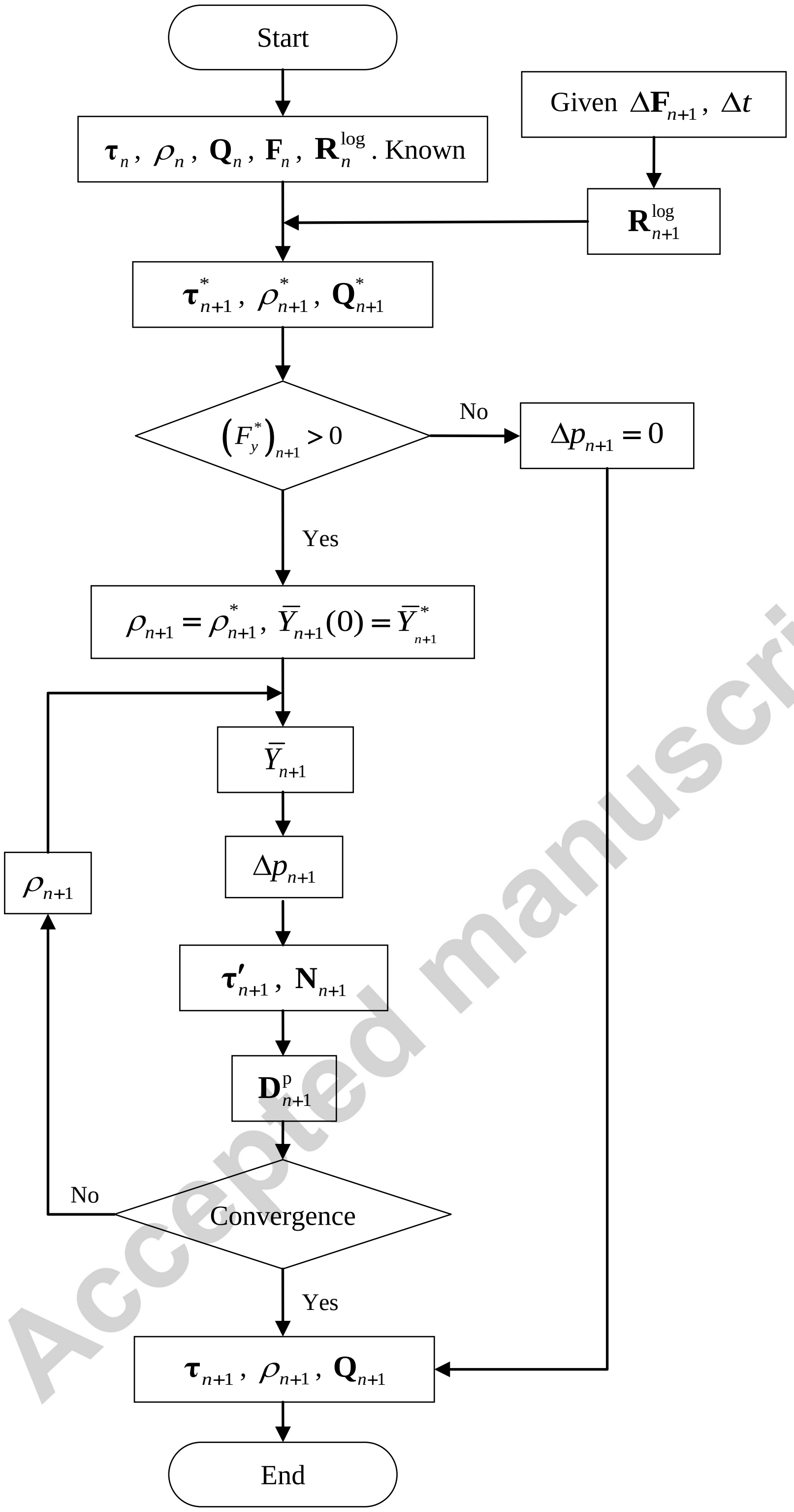

Accepted manuscript

Fig. 1. Flow chart of the stress integration algorithm of UMAT subroutine

3.3. Identification of material parameters for failure prediction

When implementing the micro-damage model into ABAQUS, the material parameters involved need to be identified. Following is the summary of the material parameters determination.

(1) The Poisson's ratio ν and initial elastic modulus E can be obtained through the uniaxial compression tests.

(2) The viscoplastic constants, K and n, can be calculated from the uniaxial compression tests at different stain rates.

(3) The initial yield stress Q_0 can be obtained from the uniaxial compression tests; the saturated stress value R^{sat} and the evolution rate β are determined by fitting the curves of τ vs. h through the following equation:

$$R = R^{sat}(1 - \exp(-\beta p)) \tag{30}$$

(4) The initial volume fraction of micro-voids f_0 can be obtained with the aid of the X-ray CT System, i.e., the total volume of the micro-voids in a selected RVE divided by the volume of the RVE.

(5) For the damage-related parameters s_1 and s_2, s_1 is considered as material-independent and the value of 2 is commonly adopted for most metallic materials [20]. s_2 can be calibrated by the hardening part of stress-strain curve.

3.4. Finite element models for cold forming of SS316L

The geometrical models of the tensile and compressive specimens with the same size of the experimental ones are shown in Fig. 2. In the FE simulations, they were simplified as 2D axisymmetric, and y-axis was the symmetric axis of the model. The models were meshed with 2D 4-node bilinear axisymmetric quadrilateral elements (CAX4). For the boundary conditions of the FE model, fixed constraint was applied on the nodes of the bottom line and the axial loading was imposed on the nodes of the

Accepted manuscript

top line. The friction coefficient of the compressive simulation was set to 0.3. The material parameters mentioned in Section 3.3 were employed in the user-defined subroutine UMAT to carry out the FE simulations.

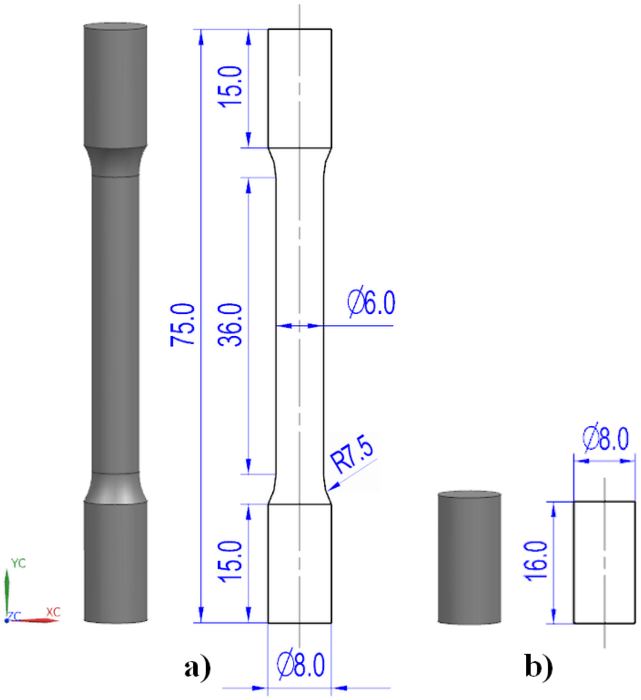

Fig. 2. Specimens designed for failure prediction in cold forming: a) tensile specimen, b) compressive specimen (dimension in mm).

4. Experiments

In this study, both uniaxial compression and tension tests were employed. The uniaxial compression test was carried out for deriving the material parameters for failure prediction, while the uniaxial tension test was performed for damage parameter calibration and experimental verification. A micro-focus X-ray CT system was specially employed to detect the micro-voids in the specimen. In such a situation, the configuration of RVE can be modelled and the VFMV can be obtained. In addition, experimental tensile and compressive stress-strain responses, as well as the

Accepted manuscript

fractographic analysis of the fractured tensile specimens, were carried out to verify the applicability of the developed micro-damage model.

4.1. Material and specimen preparation

The material used in this study was cold-rolled stainless steel SS316L bar with a diameter of 8 mm. The chemical composition of the SS316L is shown in Table 1. The specimens used for uniaxial compression and tension tests were designed according to the ASTM standard E9 – 09 and E8M – 09 respectively, i.e., cylindrical specimen with size of Ø8mm×16mm for the compression test and dog-bone shape specimen with gauge size of Ø6mm×25mm for the tension test. In order to detect the tiny internal micro-voids through the X-ray CT system, the overall size of the specimen should be designed and fabricated to be very small. Therefore, a cubic specimen with side length of around 1 mm was segmented inside the SS316L bar. It should be noted that all the compressive, tensile and CT scanning specimens were extracted from the same raw bar material to ensure the consistency of the material properties.

Accepted manuscript

Table 1 Chemical composition of SS316L (% in mass).

C	Mn	S	Si	Cr	Ni	Mo	Fe
0.02	1.46	0.004	0.03	17.58	11.05	1.42	balance

4.2. Uniaixal compression and tension tests

The uniaixal compression and tension tests were carried out on an MTS 810 testing machine at room temperature. The strains were measured using extensometers with gauge length of 10 mm and 25 mm for compression and tension tests respectively. For tension test, the applied load was controlled by the nominal strain and monotonic increased until the specimen fractured, while the load was gradually increased until a deformation of 30% was reached for the compression test. In order to predict the ductile damage behavior of the SS316L in cold forming under static or quasi-static state, the stress-strain curves at lower strain rates of 0.001 s^{-1}, 0.005 s^{-1} and 0.01 s^{-1} were obtained from both compression and tension tests. For the cold forming process under dynamic state, e.g., at high strain rates ranging from 1000 s^{-1} to 5000 s^{-1} [35], the proposed micro-damage model is still effective since the elasto-plastic behaviour and hardening behaviour of the SS316L can be described by Eqs. (2) and (30), respectively.

4.3. Determination of VFMV through micro-CT scanning

The dual-tube micro-focus X-ray CT System YXLON FF35 CT was employed to capture 2D images of the specimen with defects of micro-voids before deformation, and then to reconstruct the 3D volumetric model. The installed high-resolution transmission tube enables the system to have the capability to detect the small-sized voids up to 0.5 μm in the material. The X-ray CT scanning was carried out at 150 kV tube voltage and 60 μA tube current, the integration time was set as 400 ms and 1080 projections were generated in one full rotation. Owning to the tiny size of the specimen and nano-focus of current mode adopted, the specimen was penetrated completely by X-ray and a high-resolution of 2.7 μm was achieved. Such resolution is high enough to detect the micro-defects in the metallic materials [36, 37].

Two-dimensional (2D) projected images with three views (front, side and top views) were obtained by rotating the specimen through 360°. Subsequently, 3D volume elements were reconstructed based on appropriate algorithms with the aid of the

Accepted manuscript

ACCEPTED MANUSCRIPT

software VG Studio MAX 2.2. By defining the relative pixel intensity values of the background and material, the surface of the material was determined. Thus, the profile and inner structure of the specimen were obtained. Furthermore, by processing the voxel data of the scanned 3D CT images, information like size, number, spatial location, compactness, and sphericity of micro-voids were obtained through the defect analysis module of VGStudio MAX 2.2, then the volume of each micro-void was calculated based on their size, compactness, and sphericity [38], thus the VFMV was obtained through dividing the total volume of micro-voids in a selected RVE by the volume of the RVE. The effectiveness of the micro-damage model is highly dependent on the accuracy and reliability of the VFMV to be calculated from the information obtained through the X-ray CT System.

4.4. Fractography for fracture surfaces

The fracture surfaces of the specimens after tension tests were analyzed by using the HITACHI S-3400N SEM. The accelerating voltage was set as 20.0 kV, the current and working distances ranged from 60–150 μA and 10.5–16.8 mm respectively. Both low and high magnification images were captured for qualitatively analysis of the fracture mode and fractographical details such as micro-voids, dimples and porosities.

Accepted manuscript

5. Results and discussions

5.1. Experimental stress-strain curves

The uniaxial compressive stress-strain curves of cold-rolled SS316L at three different strain rates are shown in Fig. 3. It can be observed that the strain rate has little influence on the elastic modulus of the material whereas the measured elastic modulus is 194 GPa. However, the remarkable rate-dependence and strain-hardening effect were presented during the plastic deformation, i.e., the higher the stain rate, the greater the stress at the same measured strain. By fitting the experimental stress-strain data, the isotropic hardening parameters Q_0, R^{sat} and β, as well as the viscoplastic constants K and n, were obtained. In addition, the damage parameter s_2 was first calibrated by the hardening part of the compressive stress-strain curve and further calibrated by comparing the decline parts of the simulated and experimental tensile stress-strain curve. Table 2 shows the elastoplastic and damage parameters of the SS316L.

Accepted manuscript

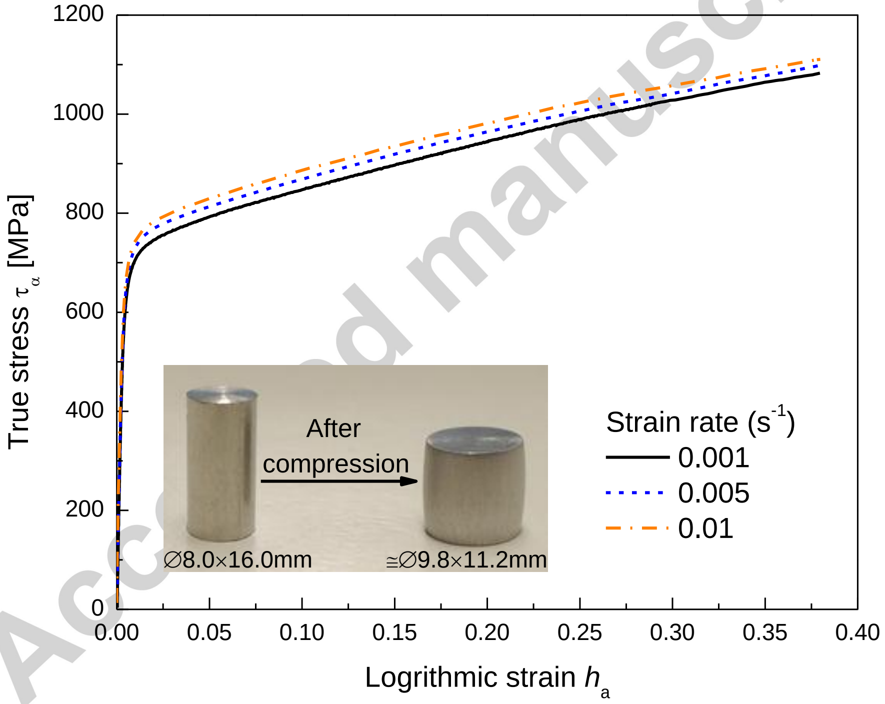

Fig. 3. Experimental compressive stress-strain curves of SS316L at different strain rates.

Table 2 Elastoplastic and damage parameters of SS316L.

ACCEPTED MANUSCRIPT

E	v	Q_0	R^{sat}	β	K	n	s_1	s_2
194 GPa	0.3	565 MPa	518 MPa	3.0	220	9.8	2	157

5.2. VFMV inside the specimen

The micro-voids of the cold-rolled SS316L specimen were detected by using our newly installed YXLON FF35 CT System. Fig. 4 shows the scanned cuboid specimen and the reconstructed 2D and 3D CT images. The relative pixel intensity value was used to determine the material surfaces of the CT images, a threshold value from image histogram was adopted to separate the micro-voids and material in the images; the micro-voids inside the specimen material were analyzed further by using the defect detection module of VGStudio MAX 2.2. To better visualize the internal micro-voids of the material, the 3D CT images of the scanned specimen were displayed semi-transparently. As shown in Fig. 4 (b), the material is represented in grey and the micro-voids with sizes ranging from 5.56 μm to 22.25 μm are represented in other different colors.

In order to study the shape, size and spatial distribution of micro-voids inside the material, three RVE models with side lengths of 750 μm, 500 μm and 250 μm were constructed from the 3D CT images, as shown in Fig. 5. The sizes distribution of micro-voids in the three RVE models are shown in Fig. 6; the results indicated that different sizes of RVE models tend to exhibit the similar trend of micro-voids distribution, i.e., following a normal distribution. The average size of micro-voids in the RVE models is around 9.8 μm, the VFMV in the RVE model was obtained by measuring the volume fraction of the micro-voids and the RVE model, and the average value is 0.000237, as shown in Fig. 7. It was also found that the average size

Accepted manuscript

and VFMV in different RVE models were similar, indicating that the micro-voids inside the cold-rolled SS316L specimen were uniformly distributed.

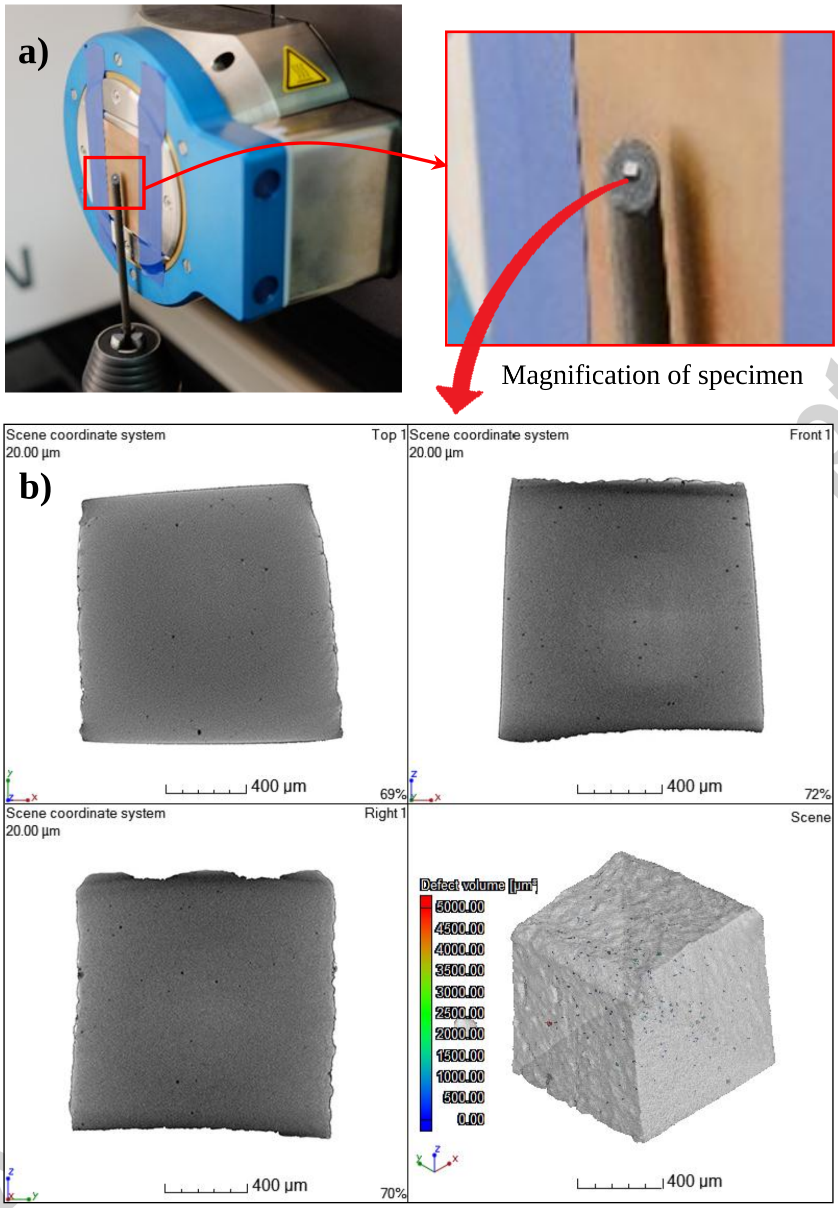

Fig. 4. X-ray CT scanning of the SS316L specimen: a) Cuboid specimen for CT scan, b) 2D and 3D CT images with micro-voids.

ACCEPTED MANUSCRIPT

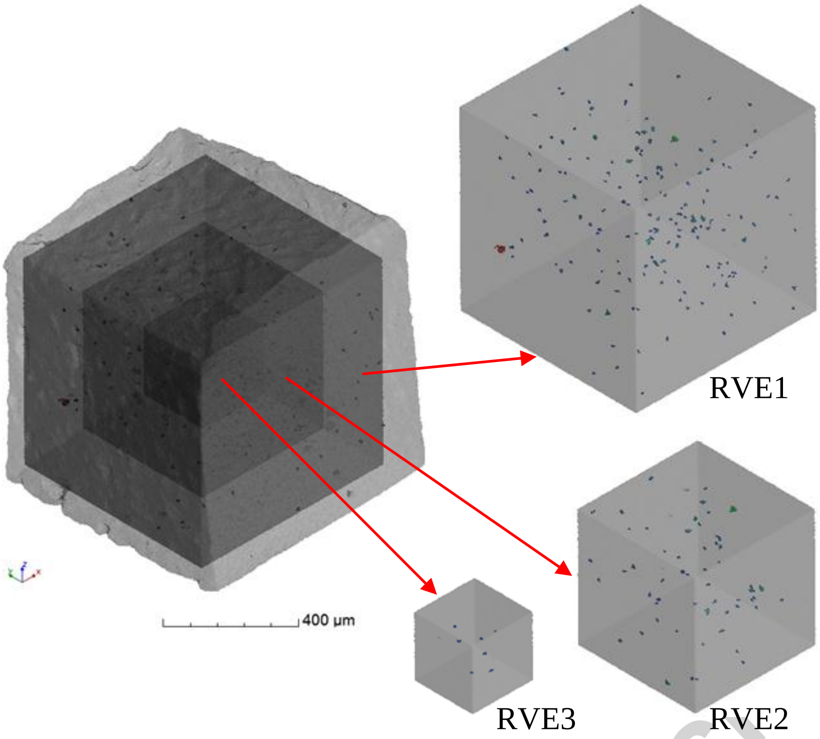

Fig. 5. Reconstruction of RVE models from the 3D CT images.

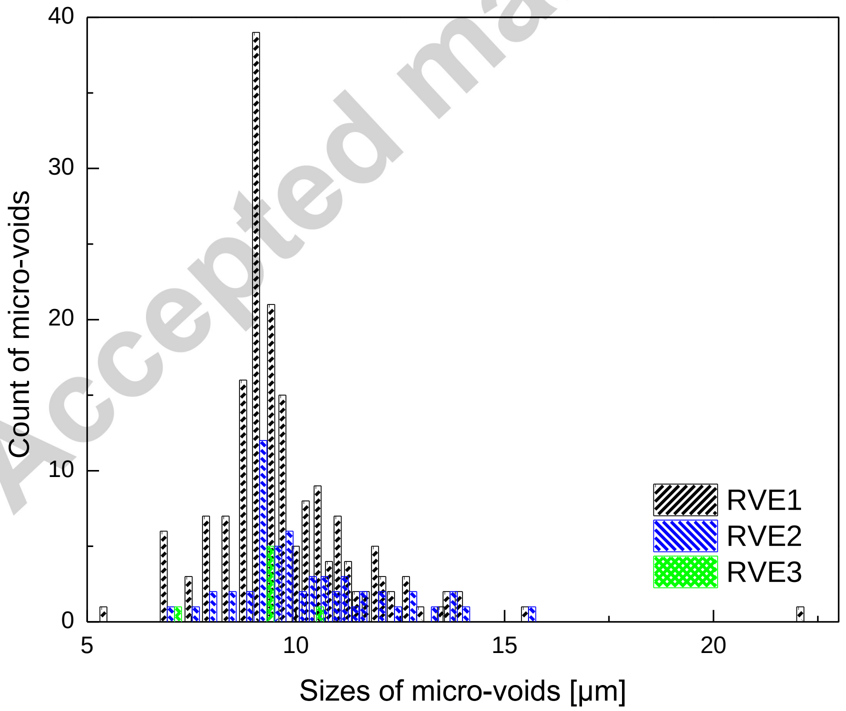

Fig. 6. Sizes distribution of micro-voids in RVE models.

Accepted manuscript

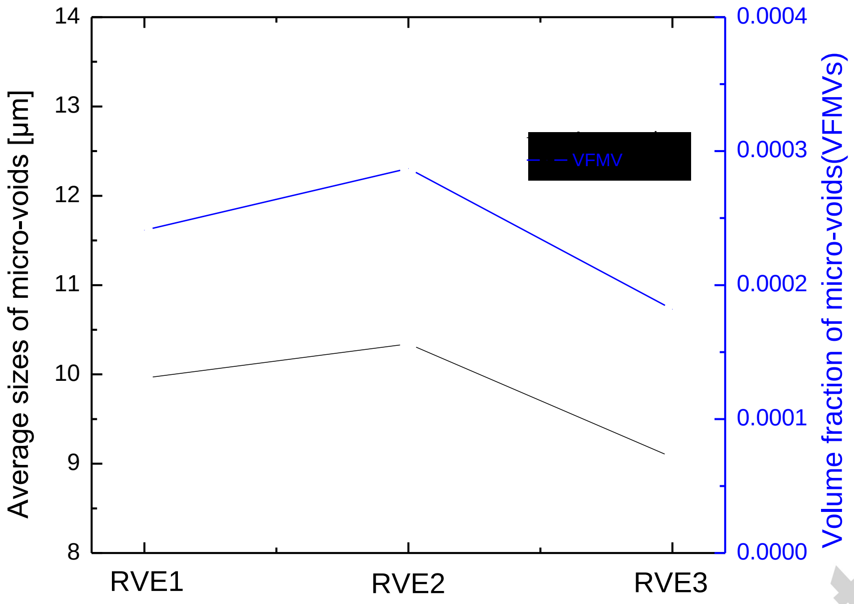

Fig. 7. Average sizes and VFMVs in RVE models.

5.3. Failure prediction in cold forming of SS316L and the verification

In this section, the stress-strain response, damage distribution and evolution of the tensile and compressive specimens at different strain rates were predicted and verificated experimentally. The experimental and predicted stress-strain curves of the SS316L specimens under uniaxial tensile deformation are shown in Fig. 8. It can be concluded that the tensile stress-strain responses of the material at different strain rates were well predicted by the micro-damage model prior to necking. Although certain discrepancies of the stresses (as shown in Fig. 8) were found after necking whereas the maximum error was around 6.9%, the onset of necking could still be predicted accurately, and the final fracture stains of the specimens under tensile tests at strain rates of 0.001 s^{-1}, 0.005 s^{-1} and 0.01 s^{-1} were 0.365, 0.308 and 0.266, respectively. It was also observed that the maximum stresses of the SS316L specimens at different strain rates were almost the same, i.e., about 1020 MPa, however, better ductility was achieved at a lower strain rate under tensile deformation.

Accepted manuscript

ACCEPTED MANUSCRIPT

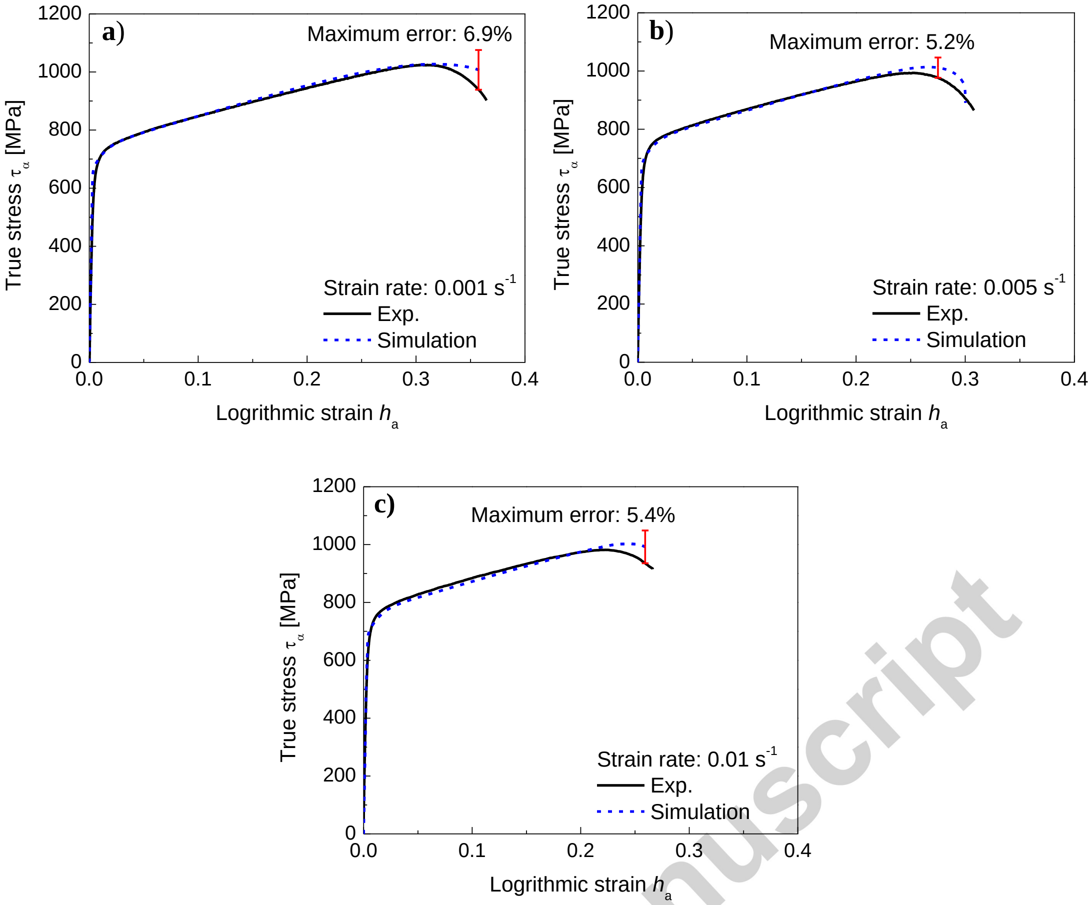

Fig. 8. Experimental and predicted stress-strain curves of SS316L specimens under uniaxial tensile deformation at strain rates of: a) 0.001 s^{-1}; b) 0.005 s^{-1} and c) 0.01 s^{-1}.

Accepted manuscript

The fractured tensile test specimens and the predicted damage distributions of tensile specimens at final fracture strains are shown in Figs. 9 and 10, respectively. It is noted that all the simulated 2D geometrical models were swept 270° along the y axis to generate 3D models for better demonstration of the internal damage distribution. In the tensile tests, localized necking occurred in each specimen. However, obvious localized necking only occurred in specimen (c) in FE simulations. The reason for this difference is that only severe damage concentration occurred at the centre region of specimen (c). The damage concentration would result in a larger deformation of the corresponding meshes in FE simulations at which localized necking occurred. It can

ACCEPTED MANUSCRIPT

be seen from Fig. 10 that higher strain rate resulted in more concentrated damage distribution, especially for specimen (c). Therefore, obvious localized necking occurred in the centre region of specimen (c), while only slight necking was found in specimens (a) and (b). Unlike the slight variation of maximum stresses, the maximum damage values of the specimen were decreased significantly with the increase of the strain rate. It should be noted that the maximum damage value indicated the allowable damage value of the specimen, i.e., the greater the allowable damage value, the stronger the ability of the material to resist fracture. Therefore, it can be concluded that the SS316L has better failure resistance at lower strain rates.

Accepted Manuscript

Fig. 9. The fractured tensile test specimens at strain rates of: a) 0.001 s^{-1}; b) 0.005 s^{-1} and c) 0.01 s^{-1}.

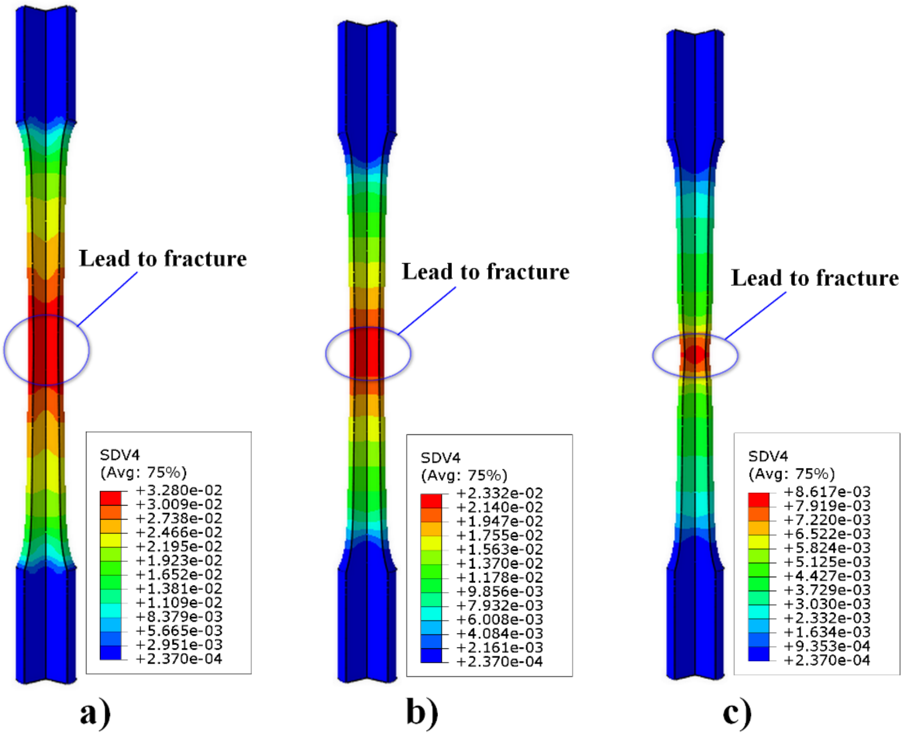

Fig. 10. The predicted damage distributions of tensile specimens at strain rates of: a) 0.001 s^{-1}; b) 0.005 s^{-1} and c) 0.01 s^{-1}.

Accepted manusc

Since the failure of the specimen is most likely to occur in the severely damaged location, the damage evolution in the centre regions of the specimens at different strain rates was analysed, as shown in Fig. 11. It can be seen that the evolution of damage followed a power function trend, i.e., the damage evolved slowly at the initial deformation stage, while increasing rapidly with the increased strain, and greater damage occurred in higher strain rate at the same strain level. In this study, the tensile simulations were performed up to the final fracture strain of each specimen. Therefore, the volume fraction of micro-voids corresponding to the final fracture strain was the critical value of micro-void evolution that led to fracture of the materials. According to the predicted results shown in Figs. 10 and 11, fracture of the materials would occur when the volume fraction of micro-voids of the tensile specimens reached

0.0328, 0.0225 and 0.00869 (these values also represent the allowable damage values) at strain rates of 0.001 s^{-1}, 0.005 s^{-1} and 0.01 s^{-1}, respectively.

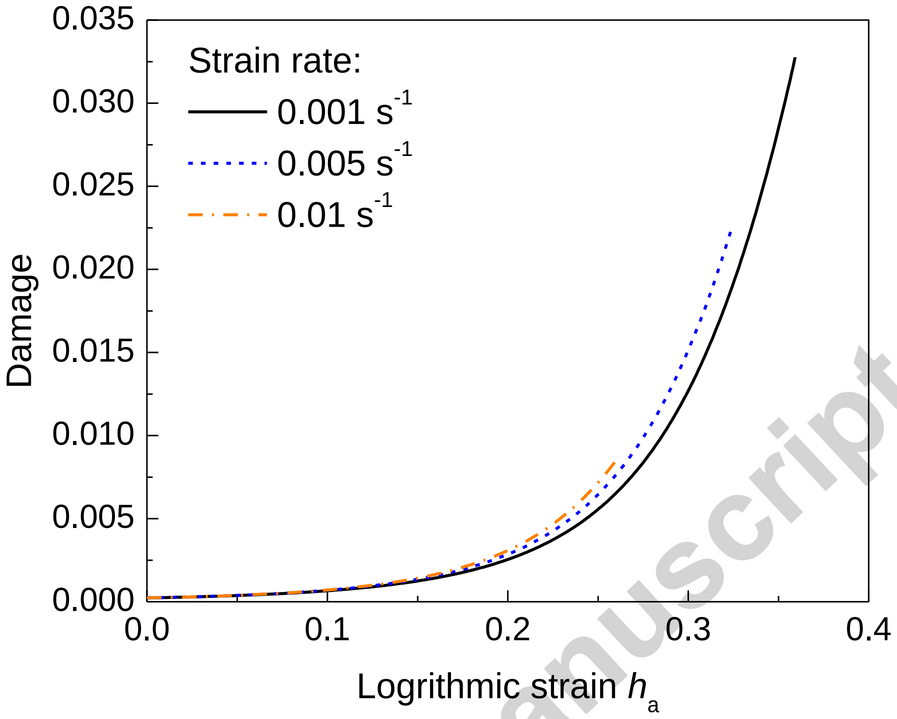

Fig. 11. Damage evolution at the centre regions of the tensile specimens at different strain rates.

Accepted manuscript

The experimental and predicted stress-strain curves of the SS316L specimens under uniaxial compressive deformation are shown in Fig. 12. It can be seen that the predicted stress-strain curves were consistent with the experimental results at different strain rates, and the maximum error was less than 2.3%. The tested and predicted damage distributions of the compressive specimens at different strain rates are shown in Fig. 13. It can be seen that the distributions of the damage at different strain rates were basically the same, and the damage was mainly distributed in the centre and the cylindrical surface of the specimens. As shown in Fig. 14, the evolution of the damage at the centre region of the specimen was very slow under compressive deformation, and the maximum damage value for all the specimens was about 0.00028, which was much smaller than that of the tensile deformation. It may be concluded that the failure was not likely to happen in this material due to the small damage accumulation during compressive deformation.

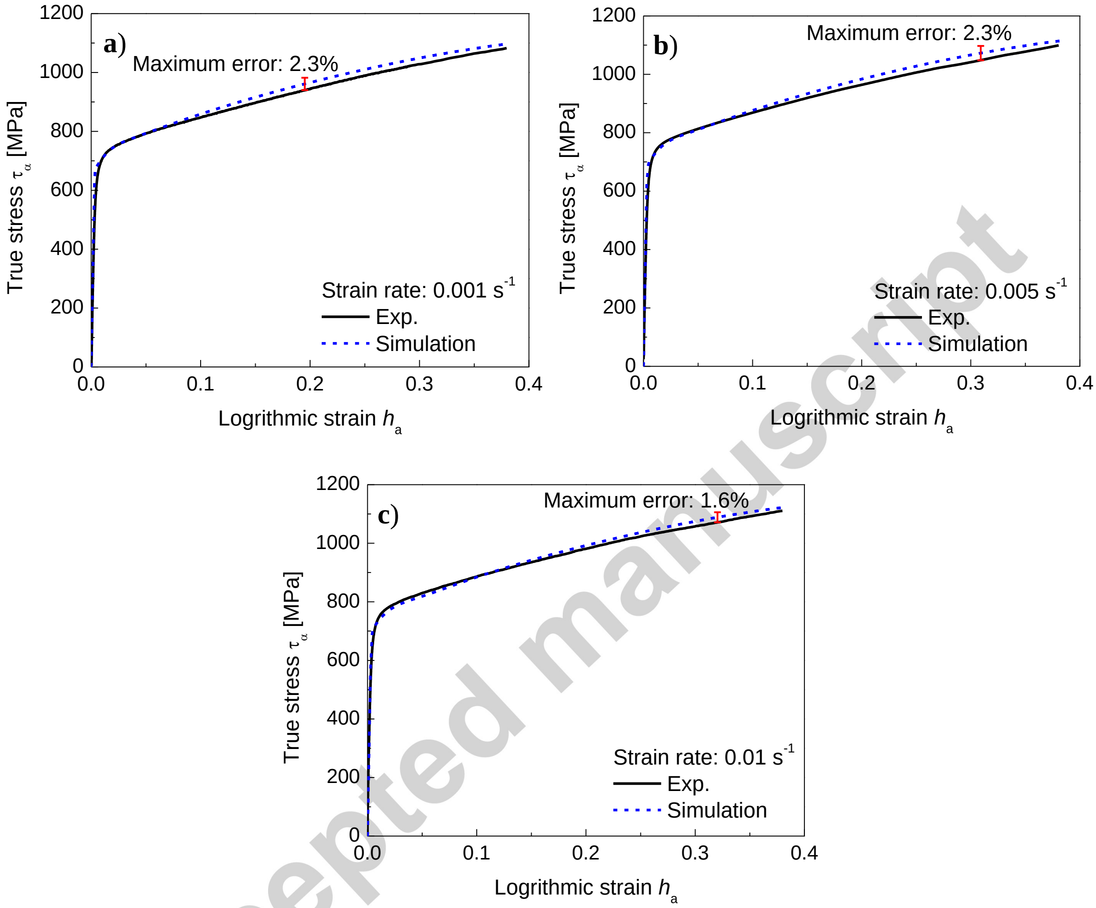

Fig. 12. Experimental and predicted stress-strain curves of SS316L specimens under uniaxial compressive deformation at strain rates of: a) 0.001 s^{-1}; b) 0.005 s^{-1} and c) 0.01 s^{-1}.

Accepted manuscript

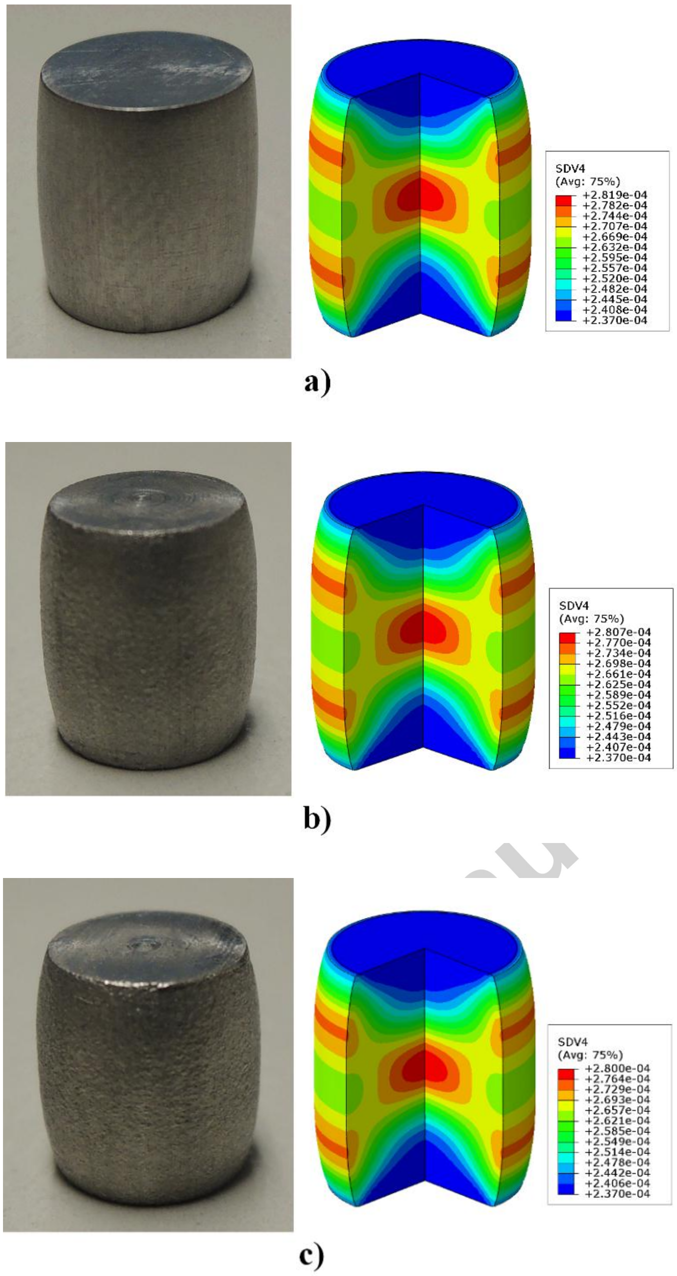

Fig. 13. The tested and predicted damage distributions of the compressive specimens at strain rates of: a) 0.001 s^{-1}; b) 0.005 s^{-1} and c) 0.01 s^{-1}.

Accepted manuscript

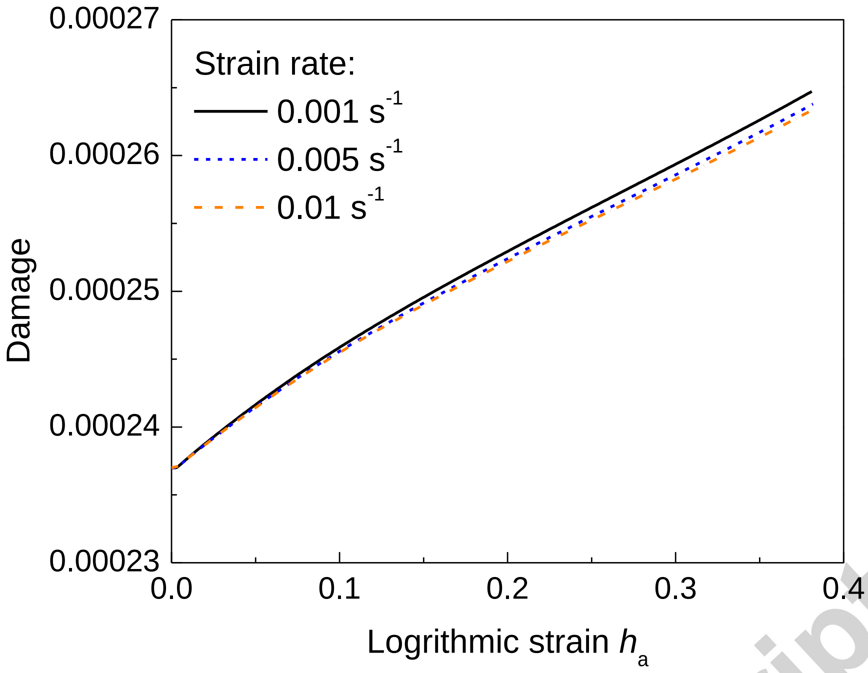

Fig. 14. Damage evolution at the centre regions of the compressive specimens at different strain rates.

Accepted manuscript

5.4. Fractographic analysis

The fractographic analysis of the fractured tensile specimens at different strain rates was performed in this study. As shown in Fig. 15, many micro-voids and dimples were found in each fracture surface, indicating that the fracture mode of the tested SS316L was ductile fracture, and the failure was largely caused by the initiation and coalescence of micro-voids in pure tension of such metallic material. It was noted that the strain rate had an obvious influence on the ductile fracture of the material. The fracture surface of the specimen, at a strain rate of 0.001 s^{-1}, was relatively flat and the size and distribution of the dimples were uniform. Several micro-void coalescence regions were shown clearly, indicating that the growth and coalescence of micro-voids can be fully formed at lower strain rates, resulting in better ductility of the material. With the increasing strain rate, the fracture sufaces of the specimens were rough and wavy (see Fig. 15 (b) and (c)), less dimples were found and their distribution was uneven, and several large, deep dimples were observed but with no obvious coalescence of micro-voids. It may be concluded that the rapid growth of the micro-void in some local regions resulted in the remaining area becoming too small to withstand the load, eventually leading to the failue of the specimen.

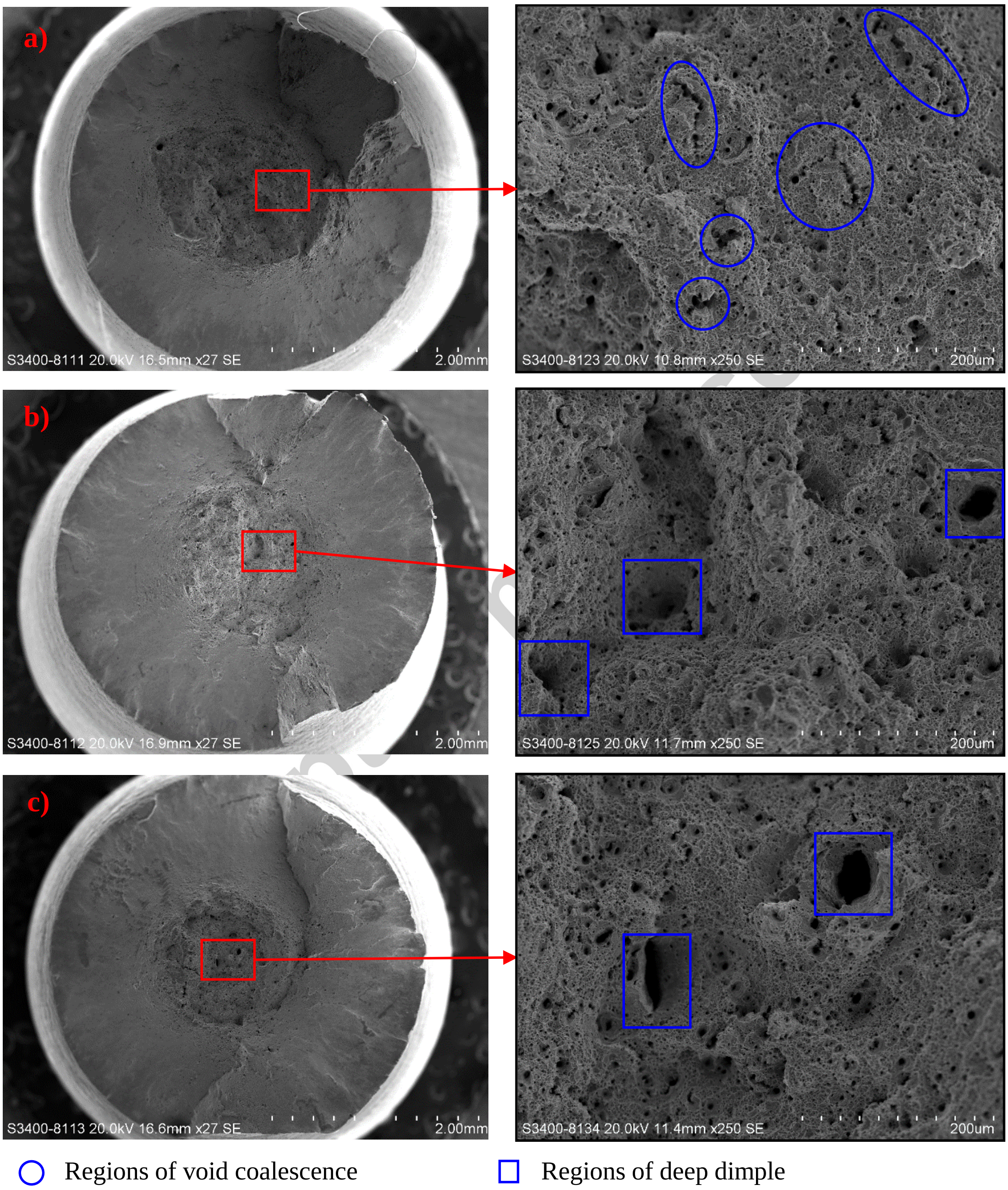

Fig. 15. SEM fractographs of the fracture surface of tensile specimens at strain of: a) 0.001 s^{-1}, b) 0.005 s^{-1} and c) 0.01 s^{-1}.

6. Conclusions

In the present work, a micromechanics-based damage model for failure prediction in large deformation of SS316L undergoing cold forming was developed. A micro-focus high-resolution X-ray CT system was employed to measure the micro-voids inside the specimen. 3D RVE models were reconstructed from the processed CT images of the specimen, and the average size and VFMV for the specimen were determined via statistical analysis. Furthermore, the micro-damage model was compiled as a user-defined material subroutine into ABAQUS. The stress-strain responses and damage evolution of specimens under tensile and compressive deformations at different strain rates were predicted. Finally, the experimental tensile and compressive stress-strain response, as well as the fractographic analysis, were carried out for experimental verification. The following conclusions can be drawn:

1. A micromechanics-based damage model that was concerned with the evolution of micro-voids was developed for failure prediction in large deformation of SS316L undergoing cold forming.
2. X-ray CT scanning was performed to detect the internal micro-voids of the specimen. The results indicated that the sizes distribution of micro-voids in different regions of the specimen tended to be similar and followed a normal distribution. The average size of micro-voids in RVE models was around 9.8 μm and the VFMV in the specimen was 0.000237.
3. For the tensile deformation, the maximum stresses of SS316L specimens at different strain rates were almost the same, i.e., about 1020 MPa. However, the allowable damage values of the specimen were decreased significantly with the increase of the strain rate, and the SS316L had better failure resistance at lower

Accepted manuscript

ACCEPTED MANUSCRIPT

strain rates. The evolution of damage in tensile deformation followed a power function trend, i.e., the damage evolved slowly at the initial deformation stage, while increased rapidly with the increasing of strain, and the greater damage occurred in higher strain rate at the same strain level.

4. For the compressive deformation, the predicted stress-strain responses of SS316L specimens at different strain rates were in good agreement with the corresponding experimental ones. The damage distribution and evolution of the specimens at different strain rates were basically the same. The evolution of damage in compressive deformation was very slow and the damage value was much smaller than that of tensile deformation. It may be concluded that the failure was not likely to happen in this material due to the small damage accumulation during compressive deformation.
5. Ductile fracture mode was found for the fractured tensile specimen. The growth and coalescence of micro-voids can be formed fully at the lower strain rate, which resulted in a better ductility of the material. With the increasing of strain rate, the rapid growth of the micro-void in some local regions resulted in the remaining area becoming too small to withstand the load, eventually leading to the failue of the specimen.

Accepted manuscript

Acknowledgments

The work described in this paper was partially supported by a grant from the Research Grants Council of the Hong Kong Special Administrative Region, China (Project no. PolyU 511511), PhD studentship (Project account code RTBN) and the Central Research Grants from The Hong Kong Polytechnic University (Project nos. G-UA70 and G-YL64). The authors would like to acknowledge Dr. Y.L. Zhu for FE modelling assistance.

ACCEPTED MANUSCRIPT

References

[1] W. Brocks, A. Cornec, I. Scheider, Computational aspects of nonlinear fracture mechanics, GKSS FORSCHUNGSZENTRUM GEESTHACHT GMBH-PUBLICATIONS-GKSS (30) (2003). http://dx.doi.org/10.1016/B0-08-043749-4/03102-5.

[2] J. Lemaitre, A continuous damage mechanics model for ductile fracture, J. Eng. Mater. Technol. 107(1) (1985) 83-89. http://dx.doi.org/10.1115/1.3225775.

[3] L. Kachanov, Introduction to continuum damage mechanics, Springer Science & Business Media1986. http://dx.doi.org/10.1007/978-94-017-1957-5.

[4] J. Lemaitre, A course on damage mechanics, Springer Science & Business Media, 2012. http://dx.doi.org/10.1007/978-3-662-02761-5.

[5] J. Lemaitre, J.-L. Chaboche, Mechanics of solid materials, Cambridge university press, 1990. http://dx.doi.org/10.1017/CBO9781139167970.

[6] T.J. Wang, Unified CDM model and local criterion for ductile fracture—I. Unified CDM model for ductile fracture, Eng. Fract. Mech. 42(1) (1992) 177-183. http://dx.doi.org/10.1016/0013-7944(92)90289-Q.

[7] J.L. Chaboche, M. Boudifa, K. Saanouni, A CDM Approach of Ductile Damage with Plastic Compressibility, Int. J. Fract. 137(1-4) (2006) 51-75. http://dx.doi.org/10.1007/s10704-005-3061-5.

[8] F.M. Andrade Pires, E.A. de Souza Neto, D.R.J. Owen, On the finite element prediction of damage growth and fracture initiation in finitely deforming ductile materials, Comput. Meth. Appl. Mech. Eng. 193(48-51) (2004) 5223-5256. http://dx.doi.org/10.1016/j.cma.2004.01.038.

Accepted manuscript

[9] C. Soyarslan, A. Tekkaya, Prevention of internal cracks in forward extrusion by means of counter pressure: a numerical treatise, Steel Res. Int. 80(9) (2009) 671-679. http://dx.doi.org/10.2374/SRI08SP170.

[10] X. Teng, Numerical prediction of slant fracture with continuum damage mechanics, Eng. Fract. Mech. 75(8) (2008) 2020-2041. http://dx.doi.org/10.1016/j.engfracmech.2007.11.001.

[11] P.J. Zhao, Z.H. Chen, C.F. Dong, Failure analysis based on microvoids damage model for DP600 steel on in-situ tensile tests, Eng. Fract. Mech. 154 (2016) 152-168. http://dx.doi.org/10.1016/j.engfracmech.2015.11.017.

[12] D.H. Allen, Homogenization principles and their application to continuum damage mechanics, Compos. Sci. Technol. 61(15) (2001) 2223-2230. http://dx.doi.org/10.1016/S0266-3538(01)00116-6.

[13] A.L. Gurson, Continuum theory of ductile rupture by void nucleation and growth: Part I—Yield criteria and flow rules for porous ductile media, J. Eng. Mater. Technol. 99(1) (1977) 2-15. http://dx.doi.org/10.1115/1.3443401.

[14] A. Needleman, V. Tvergaard, An analysis of ductile rupture in notched bars, J. M ech. Phys. Solids 32(6) (1984) 461-490. http://dx.doi.org/10.1016/00225096(84)9003 1-0.

[15] A. Needleman, A continuum model for void nucleation by inclusion debonding, J. Appl. Mech. 54(3) (1987) 525-531. http://dx.doi.org/10.1115/1.3173064.

[16] M. Gologanu, J.-B. Leblond, J. Devaux, Approximate models for ductile metals containing non-spherical voids—case of axisymmetric prolate ellipsoidal cavities, J. Mech. Phys. Solids 41(11) (1993) 1723-1754. http://dx.doi.org/10.1016/0022-5096(93)90029-F.

Accepted manuscript

ACCEPTED MANUSCRIPT

[17] T. Pardoen, J. Hutchinson, An extended model for void growth and coalescence, J. Mech. Phys. Solids 48(12) (2000) 2467-2512. http://dx.doi.org/10.1016/S0022-5096(00)00019-3.

[18] M. Rakin, Z. Cvijovic, V. Grabulov, S. Putic, A. Sedmak, Prediction of ductile fracture initiation using micromechanical analysis, Eng. Fract. Mech. 71(4) (2004) 813-827. http://dx.doi.org/10.1016/S0013-7944(03)00013-4.

[19] G. Rousselier, Dissipation in porous metal plasticity and ductile fracture, J. Mech. Phys. Solids 49(8) (2001) 1727-1746. http://dx.doi.org/10.1016/S0022-5096(01)00013-8.

[20] G. Rousselier, The Rousselier model for porous metal plasticity and ductile fracture, Handbook of Materials Behavior Models 2 (2001) 436-445. http://dx.doi.org/10.1016/B978-012443341-0/50049-1.

[21] U. Prahl, S. Bourgeois, T. Pandorf, M. Aboutayeb, O. Debordes, D. Weichert, Damage parameter identification by a periodic homogenization approach, Comput. Mater. Sci. 25(1) (2002) 159-165. http://dx.doi.org/10.1016/S0927-0256(02)00260-4.

[22] R. Bossi, F.A. Iddings, G.C. Wheeler, P. Moore, Nondestructive testing handbook, Radiographic Testing, The American Society for Nondestructive Testing, USA, 2002.

[23] M. Maleki, J. Cugnoni, J. Botsis, Multi-scale modeling of elasto-plastic response of SnAgCu lead-free solder alloys at different ageing conditions: Effect of microstructure evolution, particle size effects and interfacial failure, Mater. Sci. Eng. A 661 (2016) 132-144. http://dx.doi.org/10.1016/j.msea.2016.03.011.

[24] M. Seifi, A. Salem, D. Satko, J. Shaffer, J.J. Lewandowski, Defect Distribution and Microstructure Heterogeneity Effects on Fracture Resistance and Fatigue

Accepted manuscript

ACCEPTED MANUSCRIPT

Behavior of EBM Ti-6Al-4V, Int. J. Fatigue 94 (2016) 263-287. http://dx.doi.org/10.1016/j.ijfatigue.2016.06.001.

[25] J. Hsieh, Computed tomography: principles, design, artifacts, and recent advances, SPIE Bellingham, WA, 2009. http://dx.doi.org/10.1117/3.2197756.

[26] E. Wielewski, G. Appleby-Thomas, P. Hazell, A. Hameed, An experimental investigation into the micro-mechanics of spall initiation and propagation in Ti–6Al–4V during shock loading, Mater. Sci. Eng. A 578 (2013) 331-339. http://dx.doi.org/10.1016/j.msea.2013.04.055.

[27] V. Nguyen Van Do, C.-H. Lee, K.-H. Chang, A nonlinear CDM model for ductile failure analysis of steel bridge columns under cyclic loading, Comput. Mech. 53 (2014) 1209-1222. http://dx.doi.org/10.1007/s00466-013-0964-2.

[28] L. Gardner, The use of stainless steel in structures, Prog. Struct. Mat. Eng. 7(2) (2005) 45-55. http://dx.doi.org/10.1002/pse.190.

[29] H. Xiao, O. T. Bruhns, A. Meyers, Logarithmic strain, logarithmic spin and logarithmic rate, Acta Mech. 124(1-4) (1997) 89-105. http://dx.doi.org/10.1007/BF01213020.

[30] O. T. Bruhns, H. Xiao, A. Meyers, Self-consistent Eulerian rate type elasto-plasticity models based upon the logarithmic stress rate. Int. J. Plast. 15(5) (1999) 479-520. http://dx.doi.org/10.1016/S0749-6419(99)00003-0.

[31] Y. Zhu, G. Kang, Q. Kan, O.T. Bruhns, Logarithmic stress rate based constitutive model for cyclic loading in finite plasticity, Int. J. Plast 54 (2014) 34-55. http://dx.doi.org/10.1016/j.ijplas.2013.08.004.

[32] G. Kang, A visco-plastic constitutive model for ratcheting of cyclically stable materials and its finite element implementation, Mech. Mater. 36(4) (2004) 299-312. http://dx.doi.org/10.1016/S0167-6636(03)00024-3.

Accepted manuscript

[33] Y. Zhu, G. Kang, Q. Kan, O.T. Bruhns, Y. Liu, Thermo-mechanically coupled cyclic elasto-viscoplastic constitutive model of metals: Theory and application, Int. J. Plast 79 (2016) 111-152. http://dx.doi.org/10.1016/j.ijplas.2015.12.005.

[34] R. Krieg, D. Krieg, Accuracies of numerical solution methods for the elastic-perfectly plastic model, J. Pressure Vessel Technol. 99(4) (1977) 510-515. http://dx.doi.org/10.1115/1.3454568.

[35] W. S. Lee, T. H. Chen, C. F. Lin, W. Z. Luo, Dynamic mechanical response of biomedical 316L stainless steel as function of strain rate and temperature. Bioinorg. Chem. Appl. 2011 (2011) 1-13. http://dx.doi.org/ 10.1155/2011/173782.

[36] R. D. K. Misra, X. L. Wan, V. S. A. Challa, M. C. Somani, L. E. Murr, Relationship of grain size and deformation mechanism to the fracture behavior in high strength–high ductility nanostructured austenitic stainless steel, Mater. Sci. Eng. A 626 (2015) 41–50. http://dx.doi.org/10.1016/j.msea.2014.12.052.

[37] L. C. Chan, X. Z. Lu, K. M. Yu, Multiscale approach with RSM for stress–strain behaviour prediction of micro-void-considered metal alloy, Mater. Des. 83 (2015) 129-137. http://dx.doi.org/10.1016/j.matdes.2015.05.064.

[38] Volume Graphics GmbH, VGStudio Max 2.2 Reference Manual, Heidelberg, 2013.

Accepted manuscript